In situ electrochemical grazing incidence small angle X-ray scattering: From the design of an electrochemical cell to an exemplary study of fuel cell catalyst degradation

Marco Bogar [a,b], Ivan Khalakhan [c,**], Alessandro Gambitta [d], Yurii Yakovlev [c], Heinz Amenitsch [b,*]

[a] CERIC-ERIC C/o Elettra Sincrotrone, S.S. 14 Km 163.5, 34149 Trieste, Italy
[b] Graz University of Technology, Institute for Inorganic Chemistry, Stremayrgasse 9, 8010 Graz, Austria
[c] Charles University, Faculty of Mathematics and Physics, Department of Surface and Plasma Science, V Holešovičkách 2, 18000 Prague 8, Czech Republic
[d] Elettra-Sincrotrone Trieste, SS 14 Km 163.5, Basovizza, 34149, Italy

HIGHLIGHTS

- Electrochemical cell for *in situ* gracing incidence small angle scattering.
- Simulated cathode environment of proton exchange membranes fuel cells.
- Benchmark Pt/C catalyst film during accelerated stress tests at 1.0 and 1.5 V_{RHE}.
- Pt-particles morphology changes classified from coarsening to Ostwald ripening.
- Determination of film thickness and surface area of the Pt-particles.

GRAPHICAL ABSTRACT
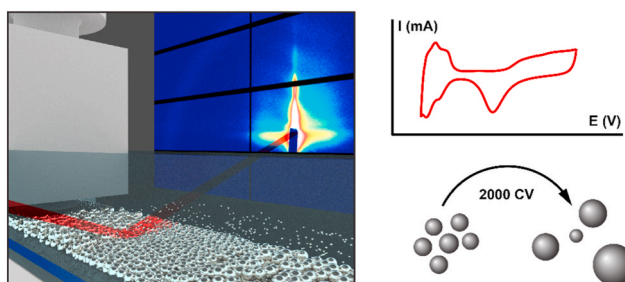
ARTICLE INFO

ABSTRACT

Nowadays, electrochemistry has a considerable technological impact, involving fuel cells, super capacitors and batteries. These devices are based on complex architectures, which complicates monitoring their evolution *in situ* under operating conditions to reveal the reasons for reduced lifetime and performances. Here, we present a design of a multipurpose electrochemical cell for grazing incidence small and wide angle X-ray scattering (GISAXS and GIWAXS) where the environment for operating conditions can be recreated. We focus on proton exchange membrane fuel cells (PEMFCs) which operational conditions are simulated by means of potentiodynamic-based accelerated stress tests, applied to a thin film of Pt nanoparticles representing a model system of a benchmark catalyst. Two different upper potentials are used to mimic fuel cell operating conditions: at 1.0 V $_{RHE}$ the catalyst film preserves its initial morphology, while at 1.5 V $_{RHE}$ (simulating fuel cell start-up/shut-down cycles) significant coarsening has been observed. The initial dimension of the Pt particles of 4.0 nm increases to 8.7 nm due to the predominant process of coalescence and final Ostwald ripening. In parallel, the distance between the particles increases, the catalyst film (9 nm thick) becomes thinner at first and exhibit a higher roughness at the end.

* Corresponding author.
** Corresponding author.
E-mail addresses: ivan.khalakhan@mff.cuni.cz (I. Khalakhan), amenitsch@tugraz.at (H. Amenitsch).

1. Introduction

Electrochemistry has a profound impact on research connected with the development and improvement of green energy power sources. In fact, the reduction-oxidation reactions play a crucial role in fuel cells [1–5], super capacitors [6] and batteries [7,8]. Thus, to improve performance in these families of devices, it is fundamental to entirely understand the electrochemistry related effects under their operational conditions. With this aim, during the last decades, various methods have been developed to adapt device architectures or create new electrochemical cells dedicated to the so-called *in situ* investigations.

For example, concerning fuel cells, catalyst stability is still a crucial factor limiting their entrance in the worldwide market. Nonetheless, studies of catalyst degradation have gained a huge boost during the last decade, a complete comprehension of deterioration dynamics and the consequent development of corresponding mitigation strategies are still missing. Specifically, when speaking about proton exchange membrane fuel cells (PEMFCs), the acidic environment and the high potentials at the cathode side constitute harmful operating conditions in which the platinum catalyst is oxidized. This oxidative process is the main contributing factor in electrocatalyst coarsening and, hence, decreasing of the electrochemically active surface area (ECSA) and consequent reduction of fuel cell performance [9]. The severity of degradation is further exacerbated by the transient and cyclic nature of PEMFCs operation. In fact, during high load operation the catalyst is in its metallic state, while during start-up/shut-down conditions, cathode catalyst is oxidized.

Up to date several closely related mechanisms leading to catalyst's ECSA decrease upon its operation have been identified: platinum dissolution which induces the so-called Ostwald ripening and carbon support corrosion responsible for platinum particle agglomeration and detachment [10]. Due to the fact that all aforementioned phenomena occur simultaneously, the complete picture of catalyst coarsening have yet to be unravelled. The current frontiers of knowledge are expected to expand with the rising of modern *in situ* techniques that are capable of measuring catalyst directly during its operation under realistic environments. A variety of *in situ* microscopic methods have been recently developed to characterize the electrified solid-liquid interface inside specially designed electrochemical cells. In this class of experimental chambers, the so-called accelerated stress tests (ASTs) are performed: they consist in potentiodynamic cycling from low to high potentials in an acidic electrolyte and have been developed to simulate catalyst degradation on a shorter timescale; simultaneously the catalyst is monitored. Powerful *in situ* transmission electron microscopy (TEM), atomic force microscopy (AFM), scanning tunnelling microscopy (STM) were successfully applied to provide online information about catalyst coarsening during ASTs [11–23].

However, microscopy-based techniques have some significant drawbacks. The probed area is quite small resulting in a poor statistics of the results. In case of AFM and STM the recorded image is a convolution of the sample morphology and the tip, providing only limited structural resolution. Last but not least, the time required to collect the image can be very long.

As a complement (or a substituent) to *in situ* microscopy, X-rays-based techniques have the advantage of high penetration depth. This facilitates the cell design in order to easily control temperature, chemical potential or electrical fields, thus creating an environment simulating *operando* conditions. Moreover, due to their specific features such as penetration, high intensity, small or large beam dimension and energy tunability, X-rays can probe large surface areas or specific small features thus providing structural and chemical information with high statistical significance. These capabilities are further boosted by the new development of 4th generation synchrotron radiation sources e.g. MAX IV [24], ESRF [25], Petra III [26].

In this framework, several techniques have been employed for advanced *operando* characterization. As an example, X-ray absorption spectroscopy [27] and X-ray computed tomography [28] allow to retrieve unique information concerning catalyst evolution. Nonetheless, small angle X-ray scattering (SAXS) is an alternative, suitable method for structural characterization of amorphous and crystalline matter which can achieve high resolution structural data from appropriate models over relatively large sample areas in a short time.

Up to now, it was shown that *in situ* electrochemical-based SAXS analysis can be used for studying batteries [29,30], fuel cells [31–33], super capacitors [4,34], deposition [35] as well as to investigate de-alloying processes [36] or electrodeposition [37]. In order to precisely observe the desired electrochemical processes, it is crucial to optimize the design of the cell for such applications.

Here, first, we present a review on the electrochemical cells dedicated to small angle X-ray scattering (SAXS) and X-ray diffraction (XRD). Subsequently, we will discuss our design of the electrochemical cell specifically optimized for GISWAXS. Finally, an exemplary experiment is conducted with this electrochemical GISAXS cell on a thin film of Pt nanoparticles representing a model system of a Pt/C benchmark catalyst for PEMFCs. This study is focused on platinum coarsening under potentiodynamic electrochemical cycling. Cyclic voltammetry is performed by using two different upper potentials (E_U) with respect to the reversible hydrogen electrode (RHE): 1.0 V_{RHE} and 1.5 V_{RHE}. These two upper voltages are representative of two different operative stages of a PEMFC: the former potential usually characterizes the high-load operation conditions, while the latter one can stress the catalyst during the start-up/shut-down stages of the device.

1.1. Previously designed electrochemical cells for in situ SAXS analysis

Generally, SAXS allows to characterize precisely the morphology of a scattering object and to monitor the evolution of a system with high temporal resolution and in a versatile environment. SAXS can be carried out in two distinct geometries, namely in transmission or at grazing incidence conditions (GISAXS). In the former case, the setup is used to investigate bulk samples, and the scattered radiation is produced from an incident beam directly crossing them. On contrary, GISAXS has been developed to investigate the evolution of nanostructures on or buried in surfaces. In the latter case, the incident beam hits the sample surface at very small glancing angles (typically lower than one degree) and the mutual interaction between matter at the surface and radiation gives rise to the scattering pattern recorded at the detector. Data analysis is later based onto separation of the in-plane contributions, which describes the modifications involving in the plane of the surface, from the out-of-plane ones, which describes modifications taking place along the direction perpendicular to the surface plane (in depth).

During the last decades, many different electrochemical cells have been designed for specific needs. As already demonstrated from the review of Brant [38], several works present electrochemical cells for XRD. On contrary, it was noted a scarce presence of works dealing with electrochemical cells for small angle X-ray scattering. Among them, the majority focuses on a multi-technique approach where SAXS is coupled with X-ray absorption spectroscopy (XAS). This approach was, for example, used by Haubold and co-workers [39] during the Nineties, when they designed a coin-like cell entirely made of Plexiglas to study oxidation-reduction reactions involving Pt. Some years later, Braun and co-workers [40] developed an electrochemical cell made in stainless steel and polypropylene with the aim to simultaneously record X-ray diffraction pattern in addition to XAS and anomalous small angle X-ray scattering, to study battery electrodes over long time periods (also days). In this device, X-ray transmission was enabled by means of two beryllium windows. Nonetheless this experimental chamber allows to combine three techniques, two limitations can be highlighted. The first is related to cell geometry, which limits the maximum angle for XRD to 45°, while the second, and more important, is related to the presence of beryllium windows. Nowadays the use of the Kapton as a constituent material for windows in medium vacuum is a standard. Kapton is not

dangerous as beryllium and it provides a lower small angle scattering background, by being almost transparent for X-ray radiation. Moreover, it is cheap, thermally stable and easily processable. A decade later a more modern project was published: by keeping the focus on the multi-technique approach, Binniger [41], Tillier [42] and co-workers realized two twin coin-like cells: the first one to be used for both SAXS or XAS experiments with synchrotron light, while the second for measuring SAXS with laboratory equipment. Due to its chemical resistance, good mechanical stability and processability, cells were made in PEEK. Windows consisted from Kapton foils and were made conductive at the inner side by means of spray coating of the studied material. These two areas were then electrically contacted by a couple of external electrodes. Nonetheless these two cells have been carefully designed, the workflow in assembling the cell is not straightforward. In fact, the conductive side of Kapton needs to be sputtered with gold before cell assembly to improve stability of the conductive layer. For this reason, a proper sputtering mask has to be realized (according to beam and sample sizes) to allow X-ray beam to pass through without adding parasitic scattering.

As shown above, transmission SAXS setup seems being predominant due to the possibility for an easy integration in a multi-technique setup, or for the most straightforward consequent data analysis. Concerning fuel cells, during the last years two different fuel cell designs for *in situ* investigation were proposed [43,44]. But, in order to monitor the evolution of the catalyst layer via SAXS, the hydration state of the membrane electrode assembly plays a crucial role [44] and could strongly reduce the signal-to-noise ratio required to observe the evolution of the lone catalyst.

In this framework, GISAXS is a valuable technique which can provide deep insights in electrochemistry, as already demonstrated by Goryachev *et al.* [45], Ruge *et al.* [46], Moehl *et al.* [37] and Khalakhan *et al.* [47]. Up to now, to the best of our knowledge there is no single paper concerning electrochemical cells properly designed to perform *in situ* electrochemical GISWAXS and propose this work also to draw attention at the unique opportunities for investigations in energy research.

1.2. Design of the electrochemical cell

This electrochemical cell (EC) was designed to record *in situ* the

evolution of a sample morphology during electrochemical experiments using GISWAXS. Particular attention was given in maximizing as much as possible the signal-to-noise ratio of both the electrical signal at the potentiostat and the X-ray scattering pattern at the detector, to provide a complete and unique combination of these two techniques. To improve the quality of the recorded scattering pattern, the thickness of the electrolyte layer, which X-rays have to cross, was minimized to limit radiation absorption in order to be operated for X-ray energies larger than 8 keV. The cell was made via 3D printing by using a Stereo-lithography Apparatus (the *Form 2* model by Formlabs [48]). This manufacturing was chosen because it allows to easily realize articulated shapes without machining a bulk material and the high resolution of the device (laser spot size: 140 μm) allows to make components with precise, submillimetric resolution. Different material solutions were tested and finally we focused on a standard Formlabs' *Grey* resin [49] that had shown good manufacturing precision with respect to the cell micro channels. Moreover, in addition to the specifications provided from the company, chemical stability to acids which are commonly used in electrochemical experiments (such as 1 M H_2SO_4 and 1 M $HClO_4$) was successfully tested.

An exploded scheme of the cell is shown in Fig. 1a. The cell is composed by a main body (1) to host the samples, two flanges (2) for sealing the reaction chamber (3), and Kapton windows (DuPont, 13 μm; 4). The downstream flange is designed in order to guarantee an output angle of 65° (Fig. 1b). This feature allows to add an additional wide angle X-ray scattering detector to the setup to record XRD (WAXS) signal up to 65°.

Inside the cell, three electrodes are used to provide typical electrochemical measurements. One platinum wire in a form of spring serves as a counter electrode. Second platinum wire contacts the sample (working electrode) top surface. It is carefully insulated to measure currents from the sample surface only (for additional information see supporting information). Finally, the third electrode is a reference electrode placed in a close vicinity to the sample surface. For experiments in which a precise recording of voltage and current is not needed (as i.e. while applying chrono-amperometry or chrono-potentiometry to induce metal dissolution) a platinum wire can be used as a quasi-reference electrode. For proper electrochemical measurements, a thin leak-free Ag/AgCl reference electrode [50] can be used. The cell can be connected to a pump
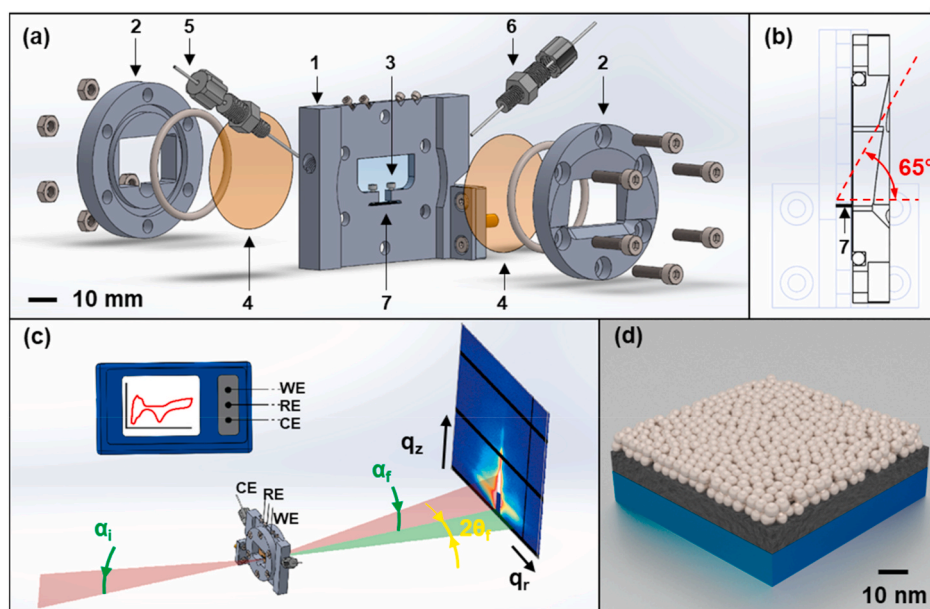

Fig. 1. Experimental setup. Sketch of the EC cell: (a) exploded scheme and (b) lateral cross-section. In (a) main components of the cell are marked by numbers: main body (1), external flanges (2), reaction chamber (3), Kapton windows (4), flow inlet (5), flow outlet (6) and sample (7, black bar); in (b) maximum exit angle is highlighted. (c) Setup of the experiment. (d) Sketch of sample composition (from bottom to top): Si substrate, C interlayer, Pt catalyst layer.

system for continuously providing a fresh electrolyte to the sample. Finally, in Fig. 1c a schematic representation of the setup is provided.

2. Experimental

Sample preparation. Pt films were prepared by means of magnetron sputtering from 2 inch Pt target (99.99% Safina) mounted on circular TORUS magnetron (K. J. Lesker) facing the substrate under the angle of 45°. Prior to the deposition, the chamber was evacuated down to 7×10^{-4} Pa. The sputtering was carried out in 0.5 Pa of Ar atmosphere in constant power mode by applying 21 W to Pt target. Total sputtering time was 7 min which forms 10 nm thin film of Pt particles. The so called Pt film was deposited on a silicon wafer (Si(111) ON Semiconductor) substrate covered by thin carbon interlayer. Carbon interlayer (10 nm) was deposited using magnetron sputtering from 4 inch graphite target (Kurt J. Lesker, purity of 99,999%) placed at a distance of 155 mm from the substrate. A DC power of 300 W was applied in Ar atmosphere with a total pressure of 0.5 Pa.

In situ **grazing incidence small angle X-ray scattering.** 2D-GISAXS patterns were recorded at the Austrian SAXS beamline at the ELETTRA synchrotron in Trieste, Italy [51]. Incident X-ray beam had a wavelength of 0.77 Å (16 keV). The sample was placed into the electrochemical cell and connected to a potentiostat (SP-240, Biologic). As a reference electrode, the leak free Ag/AgCl reference electrode (LF-1-100, Alvatek) [50] was used. The sample was placed at a distance of 194.75 cm from a pixel detector (Pilatus3 1 M, Dectris Ltd) in GISAXS geometry. The stage with the fixed cell allowed to set the glancing angle of 0.6° to the surface. The calibration was performed with Ag-behenate as a reference pattern for the GISAXS detector. For every sample, an image of the dry sample had been taken at first; then, 0.1 M H_2SO_4 solution was injected into the cell and cycling voltammetry measurements were recorded. Cyclic voltammetry was carried out from zero to the selected upper potential at room temperature with a sweep rate of 500 mV/s and for a total number of 2000 cycles. Two different upper potentials were used in total, namely 1.0 V_{RHE} and 1.5 V_{RHE}. The software IGOR Pro (IGOR Pro 7.0.8.1, Wavemetrics) was used for data reduction and fitting. Two cuts were calculated: the horizontal one, at the height of the Yoneda wings and a vertical one, along the specular condition. These two cuts have been used to calculate the correlation length [52,53] in the vertical and horizontal direction, providing sensitive information of changes of the scattering pattern.

Traces obtained from the horizontal cut were fitted via an analytical model: Pt nanoparticles were modelled as a product of the form factor and the structure factor: $I(q) \propto P(q)S(q)$. As form factor, a set of polydispersed spheres following the Schulz distribution $D_n(R)$ [54,55] was chosen: $P(q) = I_P |F(R_P, \sigma_P, q)|^2$. This term allows to retrieve information about particle shape and size distribution and to determine average particle radius, R_P, and its standard deviation, σ_P. As structure factor, the Sticky-Hard-Sphere model [56,57] was selected: $S(q) = S(R_{SHS}, \phi_{SHS}, \lambda, \varepsilon, q)$. From this term it was possible to obtain information about particle displacement on the substrate, it allowed to calculate minimum interparticle distance ($d_{P.MIN} = 2 * R_{SHS}$) and to monitor the evolution of the apparent volume fraction, ϕ_{SHS}, which is related to the probability of finding a nearest neighbour particle. For more details about the analytical model we refer to our previous work [47] in which this simplified description was developed and validated.

By combining some parameters from both, the form and structure factors, it enabled us to estimate the reduction in surface area. Despite in the analytical model used for fitting the horizontal cuts, Pt nanoparticles are modelled as spheres, particles have to be considered as ellipsoids with radius R_P and half-height H_P. Resulting particle surface area is then equal to $A_S = 4\pi R_P^2 \left(\frac{1}{2} + \frac{H_P}{2\varepsilon R_P} \arcsin(\varepsilon) \right) = 4\pi R_P^2 \chi_P$., where $\varepsilon = \sqrt{1 - H_P^2/R_P^2}$ is the eccentricity of the spheroid. Assuming that spheroid aspect ratio is not varying during particle growth, it is

possible to write particle surface area as $A_S = 2\pi R_P^2 \chi_P$, where χP is a constant defined by the aspect ratio. As previously done by Tillier *et al.* [42], it is possible to estimate surface area of platinum particles ($\widetilde{SA}$) by means of:

$$\widetilde{SA} \propto \phi_{SHS}^* A_S = \phi_{SHS}^* \int_0^\infty 2\pi \chi_P R^2 D_n(R) dR \propto$$

$$\propto \phi_{SHS}^* \int_0^\infty R^2 D_n(R) dR$$

.

Cocerning the vertical cut, the analysis was focused on the bumps characterizing the Kiessig fringes [58]. The second and the third peak of the fringes were singularly fitted and modelled as a Gaussian peak with a power law as a baseline to take into account for the particle scattering. From the spacing between these two peaks, Δq ($\Delta q = |q_2 - q_3|$; where q_x is the position of the x-th peak), thickness of the Pt layer was calculated ($t_{Pt} \cong 2\pi/\Delta q$) [59,60].

Finally, scattering length densities were calculated by means of Irina software package for IGOR Pro [61–64].

3. Results and discussion

Two samples were measured to monitor Pt coarsening induced by potentiodynamic cycling. In order to reduce the parasitic background and to simultaneously mimic the catalyst environment, first a carbon layer (10 nm thick) and then the platinum catalyst layer (10 nm thick) was sputtered onto a silicon wafer; a sketch of the sample is shown in Fig. 1d. AMF and SEM images of as deposited samples are shown in Fig. S2, revealing the Pt film morphology as catalyst nanoparticles.

The set of cyclic voltammetry (CV) cycles (from 50 to 2000 cycles) acquired during potentiodynamic cycling from 0 to 1.0 V_{RHE} and from 0 to 1.5 V_{RHE} are depicted in Fig. 2a and d, respectively. It is noteworthy that first 50 voltammetric cycles were used as the activation/cleaning treatment. The acquired CVs reveal a typical shape corresponding to pure polycrystalline platinum which demonstrates the reliability of the cell design. The left part from 0 to 0.35 V_{RHE} represents the hydrogen underpotential deposition region and the right part from 0.5 V_{RHE}, in turn, corresponds to platinum oxidation/reduction. The aforementioned regions are separated by the so-called double layer region. The applied colour code allows to follow the evolution of recorded CVs with the cycle number. At 1.0 V_{RHE} the shape of CV curves overlaps practically during all 2000 cycles. In turn, at 1.5 V_{RHE} some decrease of currents can be observed together with shift of Pt reduction peak to higher potentials. According to the literature [23,65,66] all these factor are a fingerprint of Pt coarsening.

The corresponding GISAXS horizontal and vertical cuts with identical colour code are shown in Fig. 2b and c for E_U equal to 1.0 V_{RHE} and in Fig. 2e and f for E_U equal to 1.5 V_{RHE}, respectively. With the lower potential no remarkable changes of the pattern can be highlighted. In the horizontal cut, the displacement of the Pt nanoparticles sputtered onto the surface gives rise to the structure factor peak present between 0.5 and 1.0 nm^{-1}. In the vertical cut, the presence of Kiessig fringes [58] can be clearly observed: this feature is due to the interference of the refracted X-rays at the two interfaces of the Pt layer and the periodicity of these oscillations is inversely proportional to the thickness of the Pt layer. On contrary, at E_U equal to 1.5 V_{RHE}, a remarkable evolution of the scattering patterns can be seen. In the horizontal cut (Fig. 2e) there is a clear shift of the peak from the initial position towards lower q-values, which correspond to larger dimensions in the real space. Moreover, from the vertical cut (Fig. 2f), an initial increase in Kiessig fringes periodicity can be observed, interpreted as a thinning of the Pt layer, and a successive damping of their intensity. Damping of Kiessig fringes intensity suggest a gradual destruction of the initial homogeneous structure. After
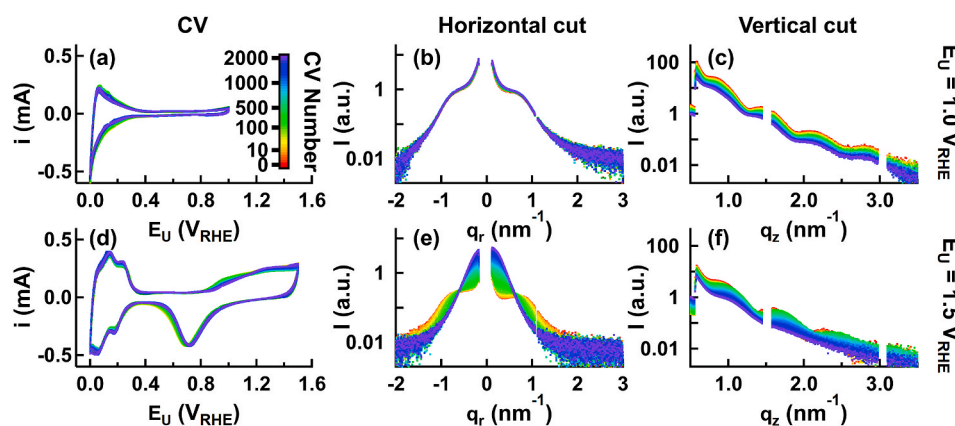
Fig. 2. *In situ* **electrochemical GISAXS.** Cycling voltammetry curves (left), GISAXS horizontal (centre) and vertical (right) cuts of time resolved electrochemical GISAXS are shown for the samples cycled over 2000 CV at the two different potentials. (a), (b), (c): E_U equal to 1.0 V_{RHE}, (d), (e), (f): E_U equal to 1.5 V_{RHE}. Note: in plots (a) and (d) CV representation is limited to the range 50–2000 cycles because the first 50 CV cycles were used as the activation/cleaning treatment. In plots (c) and (f) traces have been vertically shifted toward lower values.

800 CV cycles, only one peak characterizes the vertical cut of the scattering pattern and its position is related to the average height of the Pt nanoparticles layer.

To define the time points in which remarkable changes are taking place, the calculated scattering correlation length [52,53] represents a sensitive probe. Scattering correlation lengths calculated from horizontal (ξ_r) and vertical (ξ_z) cuts are shown in Fig. 3a and b, respectively. When the highest upper potential was used, it is possible to highlight that in-plane evolution starts after about 30 CV cycles when the slope of the correlation length becomes positive and a further upturn can be then observed around 800 CV cycles. In the same conditions, a decreasing trend of ξ_z is observed after about 30 CV cycles, which can be related to the thinning of the metallic layer. Later on, a short plateau and a successive increase starting from about 800 CV cycles follow, which can be related to the alteration of the initial structure with a consequent increase in surface roughness.

The decrease in average thickness of the Pt layer was thus quantified by determining the position of Kiessig fringes from the vertical cut; results are displayed in Fig. 3c. For the sample cycled with upper potential equal to 1.0 V_{RHE} layer thickness remains constant through the whole range. On the other hand, when the upper potential is set to 1.5 V_{RHE}, sample thickness remains constant within the first 10 cycles only. Then, a slow and continuous thinning starts taking place till 1000 CV cycles. From that point Kiessig fringes cannot be detected anymore and further analysis was not carried out. At this endpoint, a reduction in sample thickness was quantified being equal to 8% with respect the initial value.
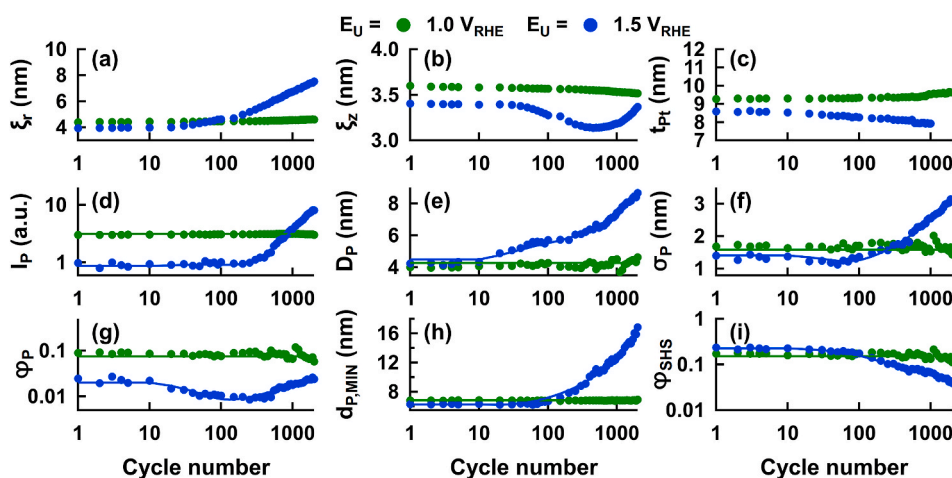
The increase of the vertical correlation length as well as the disappearance of the Kiessig fringes - both related to an increase of surface roughness - makes us assume that these changes are not only related to Pt coarsening but also partially related to carbon corrosion, which is known to take place at 1.5 V_{RHE} [10].

In order to better quantify particle evolution as a function of applied CV cycles, scattering patterns resulting from horizontal cut were fitted using the analytical model for spherical particles with size distribution and structure factor; results are shown in second and third row of Fig. 3. The linear and constant trend of the sample cycled in mild conditions (E_U equal to 1.0 V_{RHE}) is consistent with the observed stability of the catalyst material revealed from scattering patterns and cyclic voltammetry. The parameters remain constant, pointing towards the stability of the sample morphology.

However, when cycling voltammetry was performed in harsh conditions (E_U equal to 1.5 V_{RHE}), the evolution of the system can be described from the whole set of fitted parameters. After an initial and short stability within 10 and 100 CV cycles both, an increase in average particle diameter, D_P (Fig. 3e), and a decrease in particle polydispersity (related to the parameter σ_P, Fig. 3f), can be highlighted. This trend can be related to initial particles coalescence as supported from the average thinning of Pt layer. The effect of Pt dissolution and redeposition on the catalyst morphology mainly develops along the lateral direction. This growth causes the initial reduction of polydispersity and to the formation of larger particles which will later continue to grow in size. As well, after few tens of CV cycles Pt dissolution rate is supposed to increase due

Fig. 3. Parameters obtained from GISAXS. Temporal evolution of the parameters obtained from GISAXS analysis, referred to the two samples: cycled at $E_U = 1.0$ V_{RHE} (green) and at $E_U = 1.5$ V_{RHE} (blue). (a), (b) Scattering correlation length calculated: (a) from the horizontal cut, ξ_r (in the range: 0.22 ÷ 1.67 nm^{-1}) and (b) from the vertical cut, ξ_z (in the range 0.59 ÷ 2.97 nm^{-1}). (c) thickness of the Pt layer retrieved from the vertical cut, t_{Pt}. Parameters extracted from fitting the horizontal cut. Form factor parameters: (d) forward scattering intensity of Pt nanoparticles I_P, (e) average particle diameter D_P, (f) standard deviation from average particle diameter σ_P and (g) calculated volume fraction of nanoparticles ϕ_P. Structure factor parameters: (h) minimum inter-particle distance $d_{P,MIN}$ (obtained by doubling the value of the hard sphere radius, R_{SHS}) and (i) apparent volume fraction ϕ_{SHS}. Note: continuous lines were added as a guideline for the eyes only. (For interpretation of the references to colour in this figure legend, the reader is referred to the Web version of this article.)

to the exposition of a different Pt surface at the electrolyte and a decrease in total Pt volume fraction, ϕ_P (Fig. 3g) can be observed. It must be noted that due to assumption of a Schulz distribution for the number size distribution the interpretation of the volume fraction ϕ_P is qualitative only. After 100 CV cycles, parameters related to the form factor maintain their increasing trend. This increase in average particle size and volume is also reflected in continuous increase of forwarded scattering probability I_P (Fig. 3d), which is proportional to the square value of average particle volume. Concerning the structure factor, within the first 800 CV cycles it can be observed a doubling of minimum interparticle distance, $d_{P,MIN}$ (Fig. 3h), which keeps rising till the end of the experiment. On contrary, the apparent volume fraction ϕ_{SHS} (Fig. 3i), related to packing density, is reduced by one third within the first 800 CV cycles and keeps decreasing till the end of the experiment. The combination of these data suggests that the initial particle coalescence is replaced by Ostwald ripening in the late stages of the experimental range. This is supposed to be related to the continuous growth in both size and polydispersity, and overall evident after the sudden growth of the particle diameter D_P which appears around 800 CV cycles. At this stage, due to the Ostwald ripening mechanism, remnants of small Pt particles are dissolved and Pt is redeposited increasing the size of the larger particles already forming the Pt film [23,67–69]. The effects of this growth might predominantly involve the evolution along the vertical cut, as suggested from the positive slope in vertical correlation length and from visual appearance from the vertical cut. Nonetheless, it must be pointed out that the effects described till now are not only induced by dissolution/redeposition of platinum only. Carbon corrosion is also a factor which has been observed inducing modification of the substrate and particle detachment [10]. Though, in our previous studies [23] we highlighted that carbon corrosion is not clearly observable by means of scanning probe microscopy and, also in this work, the only effects which could be partly related to carbon corrosion is the roughening of the surface of the sample, which is visible from the disappearing of the Kiessig fringes in the vertical cut. The main issue related to discriminate between carbon corrosion and coarsening of catalyst layer is due to the poor scattering length density of carbon if compared to the platinum one. Calculating the corresponding electron densities for Platinum $\rho_{Pt} = 145.5 \ 10^{10} \ cm^{-2}$, and Carbon $\rho_C = 16.53 \ 10^{10} \ cm^{-2}$; the contribution of increased porosity in the carbon layer due to carbon corrosion and the Pt particle morphology to the total scattered intensity can be estimated. The intensity contributions are related to the square of the electron density differences referred to water, i.e. $\rho_{Pt-H_2O}^2 = 1.85 \ 10^{24} \ cm^{-4}$, $\rho_{C-H_2O}^2 = 5.06 \ 10^{21} \ cm^{-4}$, which results in a ratio of 370 between Pt and carbon. In other words, by considering the same layer thickness and morphology for both catalyst layer and carbon layer, the Pt-particles would scatter 370 times stronger than the same number of pores or losses of carbon material due to carbon corrosion, which let us assume that the observed effects are related to the changes of the Pt catalyst morphology. Large contribution of losses of Pt particles due to detachment induced by carbon corrosion can be excluded as the forward scattering intensity I_P increases over time (Fig. 3d).

A clear confirmation supporting this evolution in morphology can be found in our previous work [23] where identical protocols were applied to the same kind of samples and measured by means of *in situ* electrochemical AFM. Resulting images showed no changes when the cyclic voltammetry was performed in mild conditions, while bigger particles and increased interparticle distance can be clearly highlighted when harsh conditions were used and both particle coalescence and growth stimulated via Ostwald ripening have been observed. The same behaviour is also reflected in RMS roughness, correlation length and ECSA calculated from the acquired AFM images which show constant trend when cycling was carried on in mild conditions. On contrary, when upper potential was risen at 1.5 V_{RHE} it was possible to quantify a doubling in RMS roughness (from 0.90 to 1.94), almost a doubling in correlation length (from 6 to 11.35 nm) and a reduction of ECSA of 20%

upon 2000 CV cycles. GISAXS was thus found matching such a trends: in fact, in this work we revealed as well almost a doubling in correlation length (ξ_r increases from 3.93 to 7.51 nm) and a decrease in estimated particle surface area equal to 22% corresponding to the ESCA reduction.

In order to summarize the obtained results in a conclusive manner, the main parameters describing the evolution of the system are listed in Table 1 as a function of some key time points, expressed in numbers of CV cycles.

4. Conclusion

In summary, here a reliable setup for *in situ* electrochemical GIS-WAXS investigations dedicated to green energy power sources has been presented. The design of the cell is robust, efficient and particularly suited for electrochemical studies in half-cell geometry. By means of this new electrochemical cell, the morphological evolution of a Pt/C model catalyst layer of the cathode has been investigated in detail. The system has been studied undergoing cyclic voltammetry at two different upper potentials mimicking two different PEMFC operational regimes. At E_U equal to 1.0 V_{RHE}, expected stability of the catalyst was confirmed. On the other hand, at E_U equal to 1.5 V_{RHE}, the morphological modification affecting the system was monitored: in a first stage, coalescence of Pt particles has been highlighted from a preferential growth in Pt nanoparticle size occurring along the plane of the surface, together with a consequent, slight, thinning of the Pt film with high structural precision. In a successive stage, it was possible to conduct the particle growth induced by Pt dissolution and redeposition to the Ostwald ripening mechanism, providing a more advanced picture about degradation of this catalytic material. Deeper insights may be gained by using anomalous GISAXS in order to address to the scattering component generated from Pt particles only, which could be important if the amount of Pt particles is reduced to mimic better the fuel cell conditions [70,71].

The applicability of this setup can be easily extended to other research fields such as battery or super capacitors in which electrochemical process are of significant importance and the structural investigations of the electrode interface layers during operation are essential. Extensive studies regarding various fuel cell catalysts and also the initial stages of the electro-corrosion processes are currently executed.

CRediT authorship contribution statement

Marco Bogar: Conceptualization, Data curation, Investigation, Software, Formal analysis, Writing - original draft, Writing - review & editing. **Ivan Khalakhan:** Conceptualization, Data curation, Investigation, Writing - original draft, Writing - review & editing, Supervision. **Alessandro Gambitta:** Resources, Writing - review & editing. **Yurii Yakovlev:** Resources, Writing - review & editing. **Heinz Amenitsch:**

Table 1
Fitting parameters of the GISAXS pattern. Values of average particle diameter D_P, standard deviation of particle diameter σ_P, minimum inter-particle distance $d_{P,MIN}$ and calculated thickness of the Pt layer, t_{Pt}. Transcription of measurement errors was omitted because always below 0.5%.

CV cycle	Average particle diameter D_P (nm)		Diameter standard deviation σ_P (nm)		Min. inter-particle distance $d_{P,MIN}$ (nm)		Calculated film thickness t_{Pt} (nm)	
$E_{U \ (V_{RHE})}$	1.0	1.5	1.0	1.5	1.0	1.5	1.0	1.5
0	4.04	4.06	1.59	1.37	6.87	6.35	9.28	8.58
10	4.06	4.32	1.63	1.37	6.86	6.34	9.28	8.53
100	4.26	5.71	1.71	1.37	6.75	6.72	9.33	8.25
800	4.15	7.05	1.68	2.51	6.84	11.95	9.42	7.96
2000	4.63	8.66	1.43	3.11	6.94	16.87	9.60	-

Appendix A. Supplementary data

Supplementary data to this article can be found online at https://doi.org/10.1016/j.jpowsour.2020.229030.

References

[1] B.P. Ladewig, S.P. Jiang, Y. Yan, Materials for Low-Temperature Fuel Cells, 2015, https://doi.org/10.1002/9783527644308.

[2] J.R. Varcoe, P. Atanassov, D.R. Dekel, A.M. Herring, M.A. Hickner, P.A. Kohl, A. R. Kucernak, W.E. Mustain, K. Nijmeijer, K. Scott, T. Xu, L. Zhuang, Anion-exchange membranes in electrochemical energy systems, Energy Environ. Sci. 7 (2014) 3135–3191, https://doi.org/10.1039/c4ee01303d.

[3] M.C. Tucker, Progress in metal-supported solid oxide fuel cells: a review, J. Power Sources 195 (2010) 4570–4582, https://doi.org/10.1016/j.jpowsour.2010.02.035.

[4] C. Koczwara, C. Prehal, S. Haas, P. Boesecke, N. Huesing, O. Paris, Towards real-time ion-specific structural sensitivity in nanoporous carbon electrodes using in situ anomalous small-angle X-ray scattering, ACS Appl. Mater. Interfaces 11 (2019) 42214–42220, https://doi.org/10.1021/acsami.9b14242.

[5] L. Su, W. Jia, C.M. Li, Y. Lei, Mechanisms for enhanced performance of platinum-based electrocatalysts in proton exchange membrane fuel cells, ChemSusChem 7 (2014) 361–378, https://doi.org/10.1002/cssc.201300823.

[6] G.Z. Chen, Supercapacitor and supercapattery as emerging electrochemical energy stores, Int. Mater. Rev. 62 (2017) 173–202, https://doi.org/10.1080/09506608.2016.1240914.

[7] J.B. Goodenough, K.S. Park, The Li-ion rechargeable battery: a perspective, J. Am. Chem. Soc. 135 (2013) 1167–1176, https://doi.org/10.1021/ja3091438.

[8] M. Gauthier, T.J. Carney, A. Grimaud, L. Giordano, N. Pour, H.H. Chang, D. P. Fenning, S.F. Lux, O. Paschos, C. Bauer, F. Maglia, S. Lupart, P. Lamp, Y. Shao-Horn, Electrode-electrolyte interface in Li-ion batteries: current understanding and new insights, J. Phys. Chem. Lett. 6 (2015) 4653–4672, https://doi.org/10.1021/acs.jpclett.5b01727.

[9] A. Taniguchi, T. Akita, K. Yasuda, Y. Miyazaki, Analysis of degradation in PEMFC caused by cell reversal during air starvation, Int. J. Hydrogen Energy 33 (2008) 2323–2329, https://doi.org/10.1016/j.ijhydene.2008.02.049.

[10] J.C. Meier, C. Galeano, I. Katsounaros, J. Witte, H.J. Bongard, A.A. Topalov, C. Baldizzone, S. Mezzavilla, F. Schüth, K.J.J. Mayrhofer, Design criteria for stable Pt/C fuel cell catalysts, Beilstein J. Nanotechnol. 5 (2014) 44–67, https://doi.org/10.3762/bjnano.5.5.

[11] A. Zana, J. Speder, M. Roefzaad, L. Altmann, M. Bäumer, M. Arenz, Probing degradation by IL-TEM: the influence of stress test conditions on the degradation mechanism, J. Electrochem. Soc. 160 (2013) F608–F615, https://doi.org/10.1149/2.078306jes.

[12] K. Mohanraju, L. Cindrella, Impact of alloying and lattice strain on ORR activity of Pt and Pd based ternary alloys with Fe and Co for proton exchange membrane fuel cell applications, RSC Adv. 4 (2014) 11939–11947, https://doi.org/10.1039/c3ra47021k.

[13] F.J. Rodríguez Nieto, G. Andreasen, M.E. Martins, F. Castez, R.C. Salvarezza, A. J. Arvia, Scanning tunneling microscopy, voltammetry, and x-ray photoelectron spectroscopy study of the early stages of electrochemical faceting of gold (111) in aqueous sulfuric and perchloric acid, J. Phys. Chem. B 107 (2003) 11452–11466, https://doi.org/10.1021/jp0353542.

[14] L. Jacobse, Y.F. Huang, M.T.M. Koper, M.J. Rost, Correlation of surface site formation to nanoisland growth in the electrochemical roughening of Pt(111), Nat. Mater. 17 (2018) 277–282, https://doi.org/10.1038/s41563-017-0015-z.

[15] L. Jacobse, M.J. Rost, M.T.M. Koper, Atomic-scale identification of the electrochemical roughening of platinum, ACS Cent. Sci. 5 (2019) 1920–1928, https://doi.org/10.1021/acscentsci.9b00782.

[16] J. Shan, R. Lin, S. Xia, D. Liu, Q. Zhang, Local resolved investigation of PEMFC performance degradation mechanism during dynamic driving cycle, Int. J. Hydrogen Energy 41 (2016) 4239–4250, https://doi.org/10.1016/j.ijhydene.2016.01.048.

[17] S. Nagashima, T. Ikai, Y. Sasaki, T. Kawasaki, T. Hatanaka, H. Kato, K. Kishita, Atomic-level observation of electrochemical platinum dissolution and redeposition, Nano Lett. 19 (2019) 7000–7005, https://doi.org/10.1021/acs.nanolett.9b02382.

[18] Z. Siroma, K. Ishii, K. Yasuda, M. Inaba, A. Tasaka, Stability of platinum particles on a carbon substrate investigated by atomic force microscopy and scanning electron microscopy, J. Power Sources 171 (2007) 524–529, https://doi.org/10.1016/j.jpowsour.2007.06.016.

[19] J.M. Noël, Y. Yu, M.V. Mirkin, Dissolution of pt at moderately negative potentials during oxygen reduction in water and organic media, Langmuir 29 (2013) 1346–1350, https://doi.org/10.1021/la304694d.

[20] A.P. Yadav, A. Nishikata, T. Tsuru, Effect of halogen ions on platinum dissolution under potential cycling in 0.5 M H2SO4 solution, Electrochim. Acta 52 (2007) 7444–7452, https://doi.org/10.1016/j.electacta.2007.06.029.

[21] I. Khalakhan, M. Vorokhta, M. Václavů, B. Šmíd, J. Lavková, I. Matolínová, R. Fiala, N. Tsud, T. Skála, V. Matolín, In-situ electrochemical atomic force microscopy study of aging of magnetron sputtered Pt-Co nanoalloy thin films during accelerated degradation test, Electrochim. Acta 211 (2016) 52–58, https://doi.org/10.1016/j.electacta.2016.06.035.

[22] I. Khalakhan, M. Vorokhta, P. Kúš, M. Dopita, M. Václavů, R. Fiala, N. Tsud, T. Skála, V. Matolín, In situ probing of magnetron sputtered Pt-Ni alloy fuel cell catalysts during accelerated durability test using EC-AFM, Electrochim. Acta 245 (2017) 760–769, https://doi.org/10.1016/j.electacta.2017.05.202.

[23] I. Khalakhan, A. Choukourov, M. Vorokhta, P. Kúš, I. Matolínová, V. Matolín, In situ electrochemical AFM monitoring of the potential-dependent deterioration of platinum catalyst during potentiodynamic cycling, Ultramicroscopy 187 (2018) 64–70, https://doi.org/10.1016/j.ultramic.2018.01.015.

[24] P.F. Tavares, S.C. Leemann, M. Sjöström, Å. Andersson, The max iv storage ring project, J. Synchrotron Radiat. 21 (2014) 862–877, https://doi.org/10.1107/S1600577514011503.

[25] D. Chenevier, A. Joly, ESRF: inside the Extremely Brilliant Source Upgrade, Synchrotron Radiat. News., 2018, https://doi.org/10.1080/08940886.2018.1409562.

[26] R. Wanzenberg, I. Agapov, W. Brefeld, R. Brinkmann, Y.C. Chae, H.C. Chao, J. Keil, X.N. Gavaldà, R. Röhlsberger, C.G. Schroer, M. Tischer, E. Weckert, Design status of the ultra-low emittance synchrotron facility PETRA IV, AIP Conf. Proc. 2054 (2019), https://doi.org/10.1063/1.5084565.

[27] N. Ishiguro, S. Kityakarn, O. Sekizawa, T. Uruga, H. Matsui, M. Taguchi, K. Nagasawa, T. Yokoyama, M. Tada, Kinetics and mechanism of redox processes of Pt/C and Pt3Co/C cathode electrocatalysts in a polymer electrolyte fuel cell during an accelerated durability test, J. Phys. Chem. C 120 (2016), https://doi.org/10.1021/acs.jpcc.6b04437, 19642–19651.

[28] H. Matsui, N. Ishiguro, T. Uruga, O. Sekizawa, K. Higashi, N. Maejima, M. Tada, Operando 3D visualization of migration and degradation of a platinum cathode catalyst in a polymer electrolyte fuel cell, Angew. Chem. 129 (2017) 9499–9503, https://doi.org/10.1002/ange.201703940.

[29] G.O. Park, J. Yoon, E. Park, S. Bin Park, H. Kiim, K.H. Kim, X. Jin, T.J. Shin, H. Kim, W.S. Yoon, J.M. Kim, Operando monitoring of the pore dynamics in ordered mesoporous electrode materials by small angle x-ray scattering, ACS Nano 9 (2015) 5470–5477, https://doi.org/10.1021/acsnano.5b01378.

[30] G.E. Möhl, E. Metwalli, P. Müller-Buschbaum, In Operando small-angle X-ray scattering investigation of nanostructured polymer electrolyte for lithium-ion batteries, ACS Energy Lett 3 (2018) 1525–1530, https://doi.org/10.1021/acsenergylett.8b00763.

[31] M. Povia, J. Sottmann, G. Portale, K.D. Knudsen, S. Margadonna, S. Sartori, Operando SAXS/WAXS on the a-P/C as the anode for Na-ion batteries, J. Phys. Chem. C 122 (2018) 5917–5923, https://doi.org/10.1021/acs.jpcc.7b12825.

[32] T. Asset, C.J. Gommes, J. Drnec, P. Bordet, R. Chattot, I. Martens, J. Nelayah, N. Job, F. Maillard, L. Dubau, Disentangling the degradation pathways of highly defective PtNi/C nanostructures - an operando wide and small angle X-ray scattering study, ACS Catal. 9 (2019) 160–167, https://doi.org/10.1021/acscatal.8b02665.

[33] M. Povia, J. Herranz, T. Binninger, M. Nachtegaal, A. Diaz, J. Kohlbrecher, D. F. Abbott, B.J. Kim, T.J. Schmidt, Combining SAXS and XAS to study the operando degradation of carbon-supported Pt-nanoparticle fuel cell catalysts, ACS Catal. 8 (2018) 7000–7015, https://doi.org/10.1021/acscatal.8b01321.

[34] C. Prehal, C. Koczwara, N. Jäckel, A. Schreiber, M. Burian, H. Amenitsch, M. A. Hartmann, V. Presser, O. Paris, Quantification of ion confinement and desolvation in nanoporous carbon supercapacitors with modelling and in situ X-ray scattering, Nat. Energy. 2 (2017), https://doi.org/10.1038/nenergy.2016.215.

[35] S.J. Richardson, M.R. Burton, X. Luo, P.A. Staniec, I.S. Nandhakumar, N.J. Terrill, J.M. Elliott, A.M. Squires, Watching mesoporous metal films grow during templated electrodeposition with: in situ SAXS, Nanoscale 9 (2017) 10227–10232, https://doi.org/10.1039/c7nr03321d.

[36] C.J. Dotzler, B. Ingham, B.N. Illy, K. Wallwork, M.P. Ryan, M.F. Toney, In situ observation of strain development and porosity evolution in nanoporous gold foils, Adv. Funct. Mater. 21 (2011) 3938–3946, https://doi.org/10.1002/adfm.201100735.

[37] G.E. Moehl, P.N. Bartlett, A.L. Hector, Using GISAXS to detect correlations between the locations of gold particles electrodeposited from an aqueous solution, Langmuir (2020) 1–6, https://doi.org/10.1021/acs.langmuir.9b03400.

[38] W.R. Brant, S. Schmid, G. Du, Q. Gu, N. Sharma, A simple electrochemical cell for in-situ fundamental structural analysis using synchrotron X-ray powder diffraction, J. Power Sources 244 (2013) 109–114, https://doi.org/10.1016/j.jpowsour.2013.03.086.

[39] H.G. Haubold, X.H. Wang, H. Jungbluth, G. Goerigk, W. Schilling, In situ anomalous small-angle X-ray scattering and X-ray absorption near-edge structure investigation of catalyst structures and reactions, J. Mol. Struct. 383 (1996) 283–289, https://doi.org/10.1016/S0022-2860(96)09300-3.

[40] A. Braun, S. Shrout, A.C. Fowlks, B.A. Osaisai, S. Seifert, E. Granlund, E.J. Cairns, Electrochemical in situ reaction cell for X-ray scattering, diffraction and spectroscopy, J. Synchrotron Radiat. 10 (2003) 320–325, https://doi.org/10.1107/S090904950300709X.

[41] T. Binninger, E. Fabbri, A. Patru, M. Garganourakis, J. Han, D.F. Abbott, O. Sereda, R. Kötz, A. Menzel, M. Nachtegaal, T.J. Schmidt, Electrochemical flow-cell setup for in situ X-ray investigations, J. Electrochem. Soc. 163 (2016) H906–H912, https://doi.org/10.1149/2.0201610jes.

[42] J. Tillier, T. Binninger, M. Garganourakis, A. Patru, E. Fabbri, T.J. Schmidt, O. Sereda, Electrochemical flow-cell setup for in situ X-ray investigations, J. Electrochem. Soc. 163 (2016) H913–H920, https://doi.org/10.1149/2.0211610jes.

[43] I. Martens, A. Vamvakeros, R. Chattot, M.V. Blanco, M. Rasola, J. Pusa, S.D.M. Jacques, D. Bizzotto, D.P. Wilkinson, B. Ruffmann, S. Heidemann, V. Honkimäki, J. Drnec, X-ray transparent proton-exchange membrane fuel cell design for in situ wide and small angle scattering tomography, J. Power Sources 437 (2019), https://doi.org/10.1016/j.jpowsour.2019.226906.

[44] N. Martinez, G. Gebel, N. Blanc, N. Boudet, J.S. Micha, S. Lyonnard, A. Morin, Heterogeneous nanostructural aging of fuel cell ionomer revealed by operando SAXS, ACS Appl. Energy Mater. 2 (2019) 3071–3080, https://doi.org/10.1021/acsaem.8b02004.

[45] A. Goryachev, F. Carlà, J. Drnec, W.G. Onderwaater, R. Felici, P.P.T. Krause, A.H. Wonders, E.J.M. Hensen, J.P. Hofmann, Synchrotron based operando surface X-ray scattering study towards structure–activity relationships of model electrocatalysts, Chemistry 1 (2016) 1104–1108, https://doi.org/10.1002/slct.201600355.

[46] M. Ruge, J. Drnec, B. Rahn, F. Reikowski, D.A. Harrington, F. Carlà, R. Felici, J. Stettner, O.M. Magnussen, Structural reorganization of Pt(111) electrodes by electrochemical oxidation and reduction, J. Am. Chem. Soc. 139 (2017) 4532–4539, https://doi.org/10.1021/jacs.7b01039.

[47] I. Khalakhan, M. Bogar, M. Vorokhta, P. Kúš, Y. Yakovlev, M. Dopita, D.J.S. Sandbeck, S. Cherevko, I. Matolínová, H. Amenitsch, Evolution of the PtNi bimetallic alloy fuel cell catalyst under simulated operational conditions, ACS Appl. Mater. Interfaces 12 (2020) 17602–17619, https://doi.org/10.1021/acsami.0c02083.

[48] Form 2: Affordable Desktop SLA 3D Printer | Formlabs, (n.d.). https://formlabs.com/3d-printers/form-2/(accessed April 25, 2020).

[49] 3D Printing Materials for Professionals | Formlabs, (n.d.). https://formlabs.com/materials/standard/#greyscale (accessed April 25, 2020).

[50] Leak-Free Electrodes, (n.d.). https://www.alvatek.co.uk/leak-free-electrodes/ (accessed April 25, 2020).

[51] H. Amenitsch, M. Rappolt, M. Kriechbaum, H. Mio, P. Laggner, S. Bernstorff, First performance assessment of the small-angle X-ray scattering beamline at ELETTRA, J. Synchrotron Radiat. 5 (1998) 506–508, https://doi.org/10.1107/S090904959800137X.

[52] G. Porod, General Theory - Small Angle X-Ray Scattering, Acad. Press, 1982.

[53] H.M.A. Ehmann, O. Werzer, S. Pachmajer, T. Mohan, H. Amenitsch, R. Resel, A. Kornherr, K. Stana-Kleinschek, E. Kontturi, S. Spirk, Surface-sensitive approach to interpreting supramolecular rearrangements in cellulose by synchrotron grazing incidence small-angle X-ray scattering, ACS Macro Lett. 4 (2015) 713–716, https://doi.org/10.1021/acsmacrolett.5b00306.

[54] M. Kotlarchyk, S.H. Chen, Analysis of small angle neutron scattering spectra from polydisperse interacting colloids, J. Chem. Phys. 79 (1983) 2461–2469, https://doi.org/10.1063/1.446055.

[55] M. Kotlarchyk, R.B. Stephens, J.S. Huang, Study of Schultz distribution to model polydispersity of microemulsion droplets, J. Phys. Chem. 92 (1988) 1533–1538, https://doi.org/10.1021/j100317a032.

[56] R.V. Sharma, K.C. Sharma, The structure factor and the transport properties of dense fluids having molecules with square well potential, a possible generalization, Phys. A Stat. Mech. Its Appl. 89 (1977) 213–218, https://doi.org/10.1016/0378-4371(77)90151-0.

[57] D. Pontoni, S. Finet, T. Narayanan, A.R. Rennie, Interactions and kinetic arrest in an adhesive hard-sphere colloidal system, J. Chem. Phys. 119 (2003) 6157–6165, https://doi.org/10.1063/1.1601605.

[58] H. Kiessig, Untersuchungen zur Totalreflexion von Röntgenstrahlen, Ann. Phys. (1931), https://doi.org/10.1002/andp.19314020607.

[59] U.P.V.H.T. Baumbach, High-Resolution X-Ray Scattering from Thin Films to Lateral N Anostructures, second ed., 2004, https://doi.org/10.1126/science.182.4119.1329-c.

[60] A. Gibaud, S. Hazra, X-ray reflectivity and diffuse scattering, Curr. Sci. 78 (2000) 1467–1477.

[61] J. Ilavsky, P.R. Jemian, Irena: tool suite for modeling and analysis of small-angle scattering, J. Appl. Crystallogr. 42 (2009) 347–353, https://doi.org/10.1107/S0021889809002222.

[62] F. Zhang, J. Ilavsky, G.G. Long, J.P.G. Quintana, A.J. Allen, P.R. Jemian, Glassy carbon as an absolute intensity calibration standard for small-angle scattering, Metall. Mater. Trans. A Phys. Metall. Mater. Sci. 41 (2010) 1151–1158, https://doi.org/10.1007/s11661-009-9950-x.

[63] A. Nelson, Co-refinement of multiple-contrast neutron/X-ray reflectivity data using MOTOFIT, J. Appl. Crystallogr. 39 (2006) 273–276, https://doi.org/10.1107/S0021889806005073.

[64] G. Beaucage, Approximations leading to a unified exponential/power-law approach to small-angle scattering, J. Appl. Crystallogr. 28 (1995) 717–728, https://doi.org/10.1107/s0021889895005292.

[65] M. Arenz, K.J.J. Mayrhofer, V. Stamenkovic, B.B. Blizanac, T. Tomoyuki, P.N. Ross, N.M. Markovic, The effect of the particle size on the kinetics of CO electrooxidation on high surface area Pt catalysts, J. Am. Chem. Soc. 127 (2005) 6819–6829, https://doi.org/10.1021/ja043602h.

[66] C. Lafforgue, M. Chatenet, L. Dubau, D.R. Dekel, Accelerated stress test of Pt/C nanoparticles in an interface with an anion-exchange membrane - an identical-location transmission electron microscopy study, ACS Catal. 8 (2018) 1278–1286, https://doi.org/10.1021/acscatal.7b04055.

[67] C. Wagner, Theorie der Alterung von Niederschlägen durch Umlösen (Ostwald-Reifung), Zeitschrift Für Elektrochemie, Berichte Der Bunsengesellschaft Für Phys. Chemie., 1961, https://doi.org/10.1002/bbpc.19610650704.

[68] S.R. Challa, A.T. Delariva, T.W. Hansen, S. Helveg, J. Sehested, P.L. Hansen, F. Garzon, A.K. Datye, Relating rates of catalyst sintering to the disappearance of individual nanoparticles during Ostwald ripening, J. Am. Chem. Soc. 133 (2011) 20672–20675, https://doi.org/10.1021/ja208324n.

[69] N. Hodnik, M. Zorko, M. Bele, S. Hočevar, M. Gaberšček, Identical location scanning electron microscopy: a case study of electrochemical degradation of PtNi nanoparticles using a new nondestructive method, J. Phys. Chem. C 116 (2012) 21326–21333, https://doi.org/10.1021/jp303831c.

[70] J.A. Gilbert, N.N. Kariuki, X. Wang, A.J. Kropf, K. Yu, D.J. Groom, P.J. Ferreira, D. Morgan, D.J. Myers, Pt catalyst degradation in aqueous and fuel cell environments studied via in-operando anomalous small-angle X-ray acattering, Electrochim. Acta 173 (2015) 223–234, https://doi.org/10.1016/j.electacta.2015.05.032.

[71] J.P. Simon, D. Babonneau, M. Drouet, O. Lyon, Anomalous grazing incidence small-angle X-ray scattering of carbon-encapsulated Au and Cu clusters, J. Appl. Crystallogr. 42 (2009) 312–322, https://doi.org/10.1107/S0021889809007316.